Double refraction and spin splitter in normal-conductor/hexagonal-semiconductor junctions

Peng Lv,[1] Ning Dai,[1] and Qing-Feng Sun[1,2,3,*]

[1]*International Center for Quantum Materials, School of Physics, Peking University, Beijing 100871, China*

[2]*Collaborative Innovation Center of Quantum Matter, Beijing 100871, China*

[3]*CAS Center for Excellence in Topological Quantum Computation, University of Chinese Academy of Sciences, Beijing 100190, China*

(Received 21 October 2017; revised manuscript received 28 May 2018; published 18 June 2018)

In analogy with light refraction at optical boundary, ballistic electrons also undergo refraction when propagating across a semiconductor junction. Establishing a negative refractive index in conventional optical materials is difficult, but the realization of negative refraction in an electronic system is conceptually straightforward, which has been verified in graphene *p*-*n* junctions in recent experiments. Here, we propose a model to realize double refraction and double focusing of electric current by a normal-conductor/hexagonal-semiconductor junction. The double refraction can be either positive or negative, depending on the junction being *n*-*n* type or *p*-*n* type. Based on the valley-dependent negative refraction, a spin splitter (valley splitter) is designed at the *p*-*n* junction system, where the spin-up and spin-down electrons are focused in different regions. These findings may be useful for the engineering of double lenses in electronic systems and have an underlying application of spin splitter in spintronics.

DOI: 10.1103/PhysRevB.97.235425

I. INTRODUCTION

The propagation of electrons has many similarities with the propagation of light [1,2]. In two-dimensional electron gas (2DEG), where the mean free path is larger than the size of the system, ballistic electrons propagate following straight-line trajectories which is analogous to light rays. When the ballistic electrons transmit across a semiconductor junction, electrons should undergo refraction in analogy with light refraction at optical boundary with different refractive indexes [3–6]. Such phenomena can be understood simply in terms of Snell's law, where the refractive index of photons is replaced by the wave vector of electrons. Thus it is possible to manipulate electrons like photons and electron optics has attracted worldwide attention because of its underlying applications. Electron focusing, diffraction, and double-slit interference experiments are examples of electron optics which have been clearly observed in 2DEG systems [7,8].

In conventional 2DEG systems, electrostatic lenses have been demonstrated in high mobility GaAs about 30 years ago [3,4]. Since then, many works have been undertaken to obtain various electron optical devices like mirrors, prisms, lenses, and splitters [9–20]. One interesting topic of electron optics is the negative refraction [21–23], which is challenging to achieve in conventional optical systems. For photons, this behavior can be realized in optical metamaterials [24,25]. In electronic systems, negative refraction can be achieved quite straightforwardly [9,26]. For example, when electrons transmit across a *p*-*n* junction, in order to conserve the transverse component of momentum, the transverse group velocity has to change a sign between the valence bands in *p* region and the conduction bands in *n* region, hence leading to the negative refraction. Graphene has a unique band structure with a linear dispersion relation of low-lying excitations, which gives rise to many peculiar properties [27,28]. Because of the vanishing band gap and the high intrinsic mobility, graphene has also been considered as an attractive platform for studying the electron optics [9–12,29–32]. Recent experiments have clearly demonstrated the negative refraction in graphene *p*-*n* junctions [26,31]. This negative refraction can be used to design a perfect lens and has many other potential applications.

In optics, a beam of light at the anisotropic crystal interface exhibits the double refraction effects. Recently, monolayer transition-metal dichalcogenides (TMDs) have been successfully fabricated in experiments [33–37]. The TMDs (e.g., $NbSe_2$, MoS_2) exhibit Ising pairing in superconducting phase at sufficiently low temperature, with an in-plane upper critical field far above the Pauli paramagnetic limit [33–36]. This unusual behavior is attributed to the intervalley pairing protected by Zeeman-type spin-valley locking against external magnetic fields [34]. This out-of-plane Zeeman-type spin polarization of the valleys can be used to achieve double refraction in electron optics. Motivated by this, in this paper, we propose a model to realize double refraction and double focusing of electric current by a normal-conductor/hexagonal-semiconductor junction. Although the electron refraction and focusing have been investigated in many previous works [9–16], the study of double refraction and double focusing effects are still scarce at present. Our model is based on a hexagonal lattice system (like graphene or TMDs), but breaks the *A*-*B* sublattice symmetry. By introducing a spin-orbit interaction into the system, the two valleys in the Brillouin zone are no longer equivalent. When an electron is incident from the normal conductor, double refraction and double focusing occur, and the electron transmits to two different modes. The two modes have different refractive indexes due to the two valleys being inequivalent. We investigate electron optics in both the *n*-*n* junction and *p*-*n*

*sunqf@pku.edu.cn

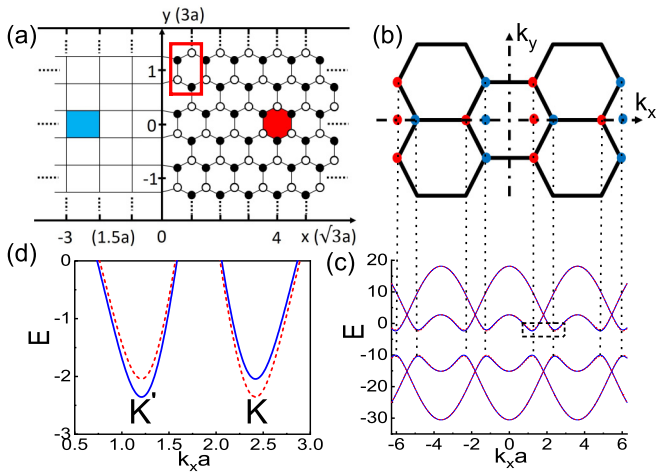

FIG. 1. Lattice diagram and band structures. (a) The schematic diagram of the normal-conductor/hexagonal-semiconductor junction in the lattice model. (b) Brillouin zone of the hexagonal lattice. (c) Energy bands along the dashed line in (b) with $k_y = 0$. Dashed red lines denote the energy bands of spin-up electrons, while the blue lines are the spin-down bands. (d) Zoom-in figure of the energy bands of the dotted box in (c). The parameters are $\epsilon_R = -6.2, t_R = -8, \beta = 4$, and $\beta_s = -0.03$.

junction below. In particular, the incident electron undergoes double negative refraction in the p-n junction. We also show that by double negative refraction with elaborately tuning the chemical potential of the system, the p-n junction can work as a spin splitter (valley splitter), which may be useful in spintronics (valleytronics).

The rest of this paper is organized as follows. In Sec. II, we present the model Hamiltonian and the corresponding band structures of the normal-conductor/hexagonal-semiconductor junction, considering both the effects of A-B sublattice symmetry breaking and spin-orbit interaction. In Sec. III, we investigate the positive double refraction in n-n junction and the negative double refraction in p-n junction. In Sec. IV, a spin splitter is designed based on the negative double refraction. Finally, a brief summary is presented in Sec. V. Appendixes A and B show that the double refraction and double focusing effects are not affected by the coupling Hamiltonian and the normal conductor. Some calculation details are presented in Appendixes C–E.

II. MODEL HAMILTONIAN AND BAND STRUCTURES

In the following, we introduce the model Hamiltonian and demonstrate the corresponding band structures. Figure 1(a) is the lattice model of the normal-conductor/hexagonal-semiconductor junction, which consists of a square lattice at the left side and a hexagonal lattice at the right side. The nearest-neighbor distance of the hexagonal lattice is set to be a and other lattice parameters are labeled in Fig. 1(a). The Hamiltonian of the whole system can be written as

$$H = H_L + H_R + H_T, \tag{1}$$

where H_L, H_R, and H_T are the Hamiltonians of the normal conductor, hexagonal semiconductor, and the coupling between them, respectively. For the normal conductor, we consider the square lattice model with the dispersion relation of its carrier being quadratic. In the tight-binding representation, the Hamiltonian H_L is of the form [38,39]

$$H_L = \sum_{i\sigma} \epsilon_L a^\dagger_{i\sigma} a_{i\sigma} + \sum_{\langle ij\rangle\sigma} t_L a^\dagger_{i\sigma} a_{j\sigma}, \tag{2}$$

where $a_{i\sigma}$ and $a^\dagger_{i\sigma}$ are the annihilation and creation operators at the discrete site i and ϵ_L is the on-site energy. The second term in Eq. (2) is the nearest-neighbor hopping. t_L is the hopping energy, which is positive for valence bands and negative for conduction bands.

Experimentally, it is possible to break the A-B sublattice symmetry in a hexagonal lattice like graphene. For example, isolated graphene/BN bilayers break the chemical equivalence of graphene A and B lattice sites [40,41]. Graphene growth on the reconstructed surface of MgO(111) also leads to A-B sublattice symmetry breaking [42,43]. In addition, spin-orbit interaction can also play a very important role in some two-dimensional materials. The emergence of the quantum spin Hall effect and topological insulators can be attributed to the rise of the spin-orbit interaction [44–47]. Thus we consider a general Hamiltonian at the hexagonal lattice side as [48]

$$H_R = \sum_{i\sigma} (\epsilon_R + \lambda_i \beta) b^\dagger_{i\sigma} b_{i\sigma} + \sum_{\langle ij\rangle\sigma} t_R b^\dagger_{i\sigma} b_{j\sigma} + \sum_{\langle\langle ij\rangle\rangle\sigma\sigma'} i\beta_s \nu_{ij} s^z_{\sigma\sigma'} b^\dagger_{i\sigma} b_{j\sigma'}, \tag{3}$$

where $b_{i\sigma}$ and $b^\dagger_{i\sigma}$ are the annihilation and creation operators at the discrete site i of the right side. ϵ_R is the on-site energy and β represents the energy difference between A-B sublattice. Here $\lambda_i = \pm 1$ for $A(B)$ sublattice. The second term is the nearest-neighbor hopping term and t_R is the hopping energy. The third term is the spin-orbit interaction which connects the second nearest neighbor. The same term also appears in the seminal work of the quantum spin Hall effect in graphene [44]. s_z is a Pauli matrix representing the electron's spin and $\nu_{ij} = -\nu_{ji} = \pm 1$ depending on the orientation of the two site i to j [44]. The spin-orbit coupling β_s is usually very small compared to t_R, but it can be in the order of meV by the Bi-cluster deposition [49]. The Hamiltonian H_T of the coupling between the left and right lead is [50–52]

$$H_T = \sum_{ij\sigma} t_c a^\dagger_{i\sigma} b_{j\sigma} + \text{H.c.}, \tag{4}$$

where t_c is the coupling strength, and we set $t_c = t_L$ throughout the work for simplicity. Note that the detailed forms of H_L and H_T and the value of t_c will not affect the results (see Appendixes A and B) [50–52]. As long as H_L is a square lattice (normal conductor), the double refraction and the double focusing effects can always occur in the normal-conductor/hexagonal-semiconductor junction. Here we assume that the interface of the normal conductor and hexagonal semiconductor are perfect [see Fig. 1(a)], which means that the interface is relatively clean and the translational invariance along the y direction persists in the system. As usual, there are defects in the real devices and the interface is rough as well. When the incident and refractive electrons are in the bottom

of the conduction band or the top of the valence band, their wavelengths are usually very long. As long as the wavelength is much longer than the defect size and the interface roughness, the direction of the refraction can be well maintained and the results are barely affected by the defect and the imperfect interface. It is worth mentioning that here the square lattice is coupled to the armchair edge of the hexagonal lattice. If the square lattice is coupled to the zigzag edge (i.e., the hexagonal lattice is rotated by 30°), only the single refraction and single focusing can occur, because of the anisotropy of the hexagonal lattice.

The Brillouin zone of the hexagonal lattice is demonstrated in Fig. 1(b). We choose each unit cell containing four atoms [see red box in Fig. 1(a)], which can simplify the calculations of the transmission coefficients; hence the Brillouin zone is one-half smaller than the usual Brillouin zone of graphene. In Fig. 1(c), we plot the energy bands along the dashed line in Fig. 1(b) with $k_y = 0$. Because of the Brillouin zone being half smaller, the number of the energy bands is doubled and each spin orientation has four energy bands. Breaking the A-B sublattice symmetry induces a big energy gap at the K and K' points. We mainly consider the electron transport near the Fermi surface and the four lower energy bands can be ignored, as they are much below the Fermi surface $E = 0$. In Fig. 1(d), the zoom-in figure of the energy bands near the K and K' points are presented. The spin-orbit coupling can be viewed as an effective magnetic field $\boldsymbol{B}$ that points in the opposite directions at the K and K' points. At K point, spin-up electrons have lower energy, while at K' point it is the other way around. Thus, for energy bands with a definite spin orientation, the energy dispersion relation between the K and K' points are no longer equivalent. In fact, this energy band is the same as that of TMDs in the normal phase [37]. So a junction consisting of a normal conductor coupled to the TMDs can be regarded as a real example of our model. In addition, the present model can also be realized in a general hexagonal lattice as long as the sublattice symmetry is broken and in the presence of the spin-orbit coupling. Double refraction occurs when electrons incident from normal conductor with square lattice transmit to the two valleys, as demonstrated in the next section.

III. DOUBLE REFRACTION AND DOUBLE FOCUSING

In this section, we demonstrate how the normal-conductor/hexagonal-semiconductor junction leads to the double refraction and double focusing. Due to the Pauli matrix σ_z commuting with the Hamiltonian in Eq. (1), the spin in the z direction is conserved in the scattering process. So, in the following analysis, we first consider a spin component, e.g., spin-up one. Figures 2(a) and 2(b) respectively illustrate the band diagrams of the n-n junction and p-n junction for a spin component and the corresponding equienergy lines in the k_x-k_y plane are shown in Figs. 2(c) and 2(d). For an incident carrier (electron or hole) from the left normal conductor, there are two beams of outgoing electrons, due to the two nonequivalent valleys. Notice that the directions of the two beams of outgoing electrons are usually different. So the double refraction occurs in this normal-conductor/hexagonal-semiconductor junction. Because of the transverse translation invariance in the model, the transverse component of the momentum (k_y) is conserved

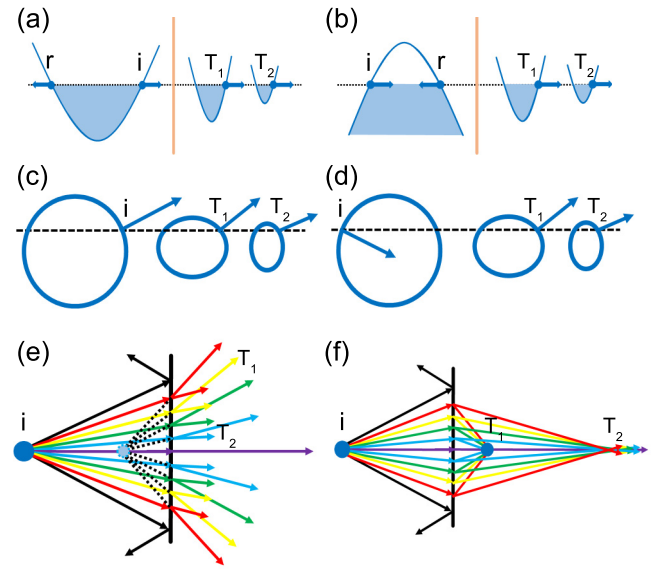

FIG. 2. Heterojunction band diagrams and schematic of double refraction. (a) The band diagrams of the n-n junction. Incident electron i transmits to the two valleys with the transmission coefficients T_1 and T_2. (b) The corresponding p-n junction case. Panels (c) and (d) are the corresponding equienergy lines in the k_x-k_y plane for the n-n junction in (a) and the p-n junction in (b). Here the arrows indicate the directions of the incident and refraction carriers. (e) Schematic of the double positive refraction in the n-n junction. Electrons emitted from the source i are bent different amounts at the n-n junction interface and two virtual focal spots are formed at the same side of the electron source. Only one virtual focal spot is plotted in (e). (f) Schematic of the double negative refraction in the p-n junction. Electrons emitted from the source i undergo double negative refraction at the p-n junction interface and two real focal spots are formed at the opposite side of the electron source.

when electrons transmit across the junction. So the transverse group velocity preserves the sign between the n-n junction [see Fig. 2(c)], but changes a sign between the valence bands in the p region and the conduction bands in the n region [see Fig. 2(d)]. As a consequence, the double refraction is positive in a n-n junction, while negative in a p-n junction. Figures 2(e) and 2(f) are the schematic diagrams of the positive and negative double reflections, respectively. For the positive double refraction, the outgoing electrons are bent different amounts as they pass through the junction and two virtual focal spots are formed at the same side of the electron source i. However, in Fig. 2(f), two real focal spots are formed at the opposite side of the electron source, attributing to the opposite transverse velocity and the negative refractive index.

To further investigate the nature of the double refraction, we calculate the transmission coefficients and the refractive indexes for both cases in detail. By applying the nonequilibrium Green's function method to the tight-binding Hamiltonian H in Eq. (1), the transmission coefficients T_1 and T_2 can be obtained quite straightforwardly by following the same procedure as in Refs. [53,54]. Figure 3 displays the case of the double positive refraction in a n-n junction, where (a) and (b) are the transmission coefficients and (c) and (d) are the refractive indexes. For small incident angle, the transmission coefficient T_1 is nearly

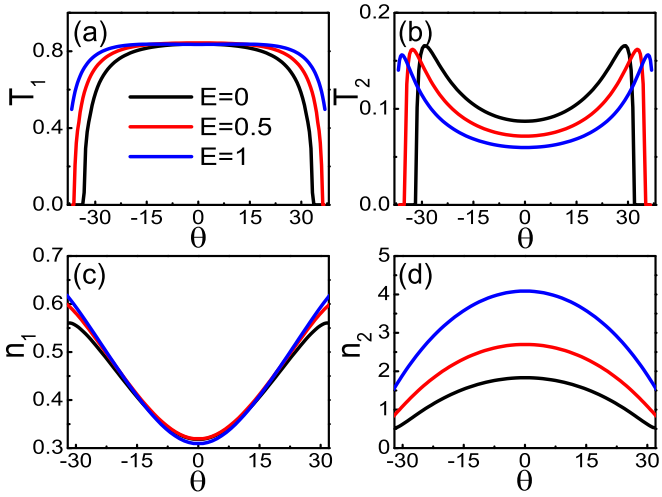

FIG. 3. Transmission coefficients and refractive indexes for the n-n junction. Panels (a) and (b) are the transmission coefficients T_1 and T_2 at the two valleys as a function of the incident angle θ for different incident energy E. Panels (c) and (d) are the corresponding refractive indexes. The parameters are $\epsilon_L = 7$, $t_L = -8$; others are the same as those in Fig. 1.

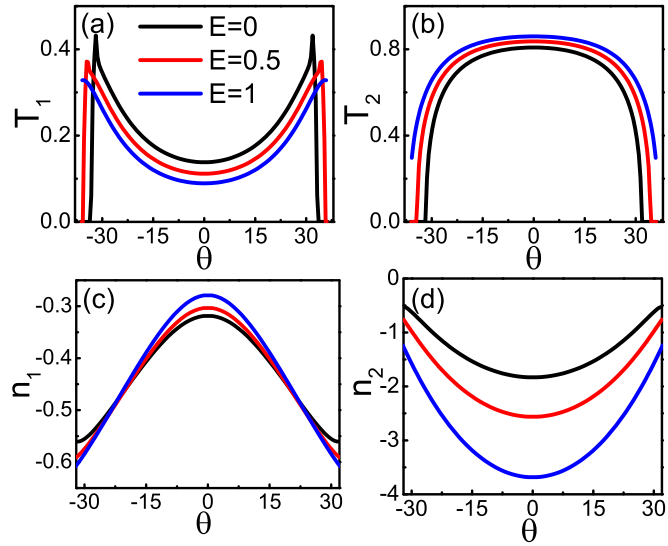

FIG. 4. Transmission coefficients and refractive indexes for the p-n junction. Panels (a) and (b) are the transmission coefficients T_1 and T_2 at the two valleys versus the incident angle θ for different incident energy E. Panels (c) and (d) are the corresponding refractive indexes. The parameters are $\epsilon_L = -7$, $t_L = 8$; others are the same as those in Fig. 1.

a constant and is insensitive to the incident energy E. As the incident angle increases, T_1 rapidly reduces and T_2 significantly increases. For large incident angle, both T_1 and T_2 drop to zero, attributing to the absence of the corresponding transmission modes at the n side. Thus electrons undergo total reflection at large incident angle. Note that T_1 dominates the whole scattering process for a large range of parameters. The increase of the incident energy enhances T_1 at large incident angle, but meanwhile suppresses the transmission coefficient T_2. The total transmission probability $T = T_1 + T_2 \approx 1$ indicates that the n-n junction is almost transparent for electrons. Meanwhile, the two transmission modes have different refractive properties as shown in Figs. 3(c) and 3(d). Here the refractive index is defined as $n_i = \sin\theta/\sin\theta_i$, where θ is the incident angle and θ_i $(i = 1,2)$ is the refraction angle of transmission mode i (for details, see Appendix C). The refractive index n_1 is insensitive to the incident energy and increases as the incident angle grows. We emphasize that $n < 1$ for a large range of parameters; hence the electronic refraction at this valley serves as an optically thinner medium in optics. For a perfect virtual focus, the refractive index n obeys the law $n^2 = c + (1-c)\sin^2\theta$ (see Appendix D), where the parameter $0 < c < 1$ in optically thinner medium. The refractive index n_1 approximately follows this law; hence this virtual focus is nearly perfect [see Fig. 2(e)]. For the refraction at the other valley, the refractive index $n > 1$ for a large range of parameters; hence electronic refraction at this valley serves as an optically denser medium in optics. Here $c > 1$ in the optically denser medium. Although n_2 is sensitive to incident energy, it also approximately matches the law $n^2 = c + (1-c)\sin^2\theta$. Therefore, the second virtual focus is also relatively good [the second virtual focal spot is not plotted in Fig. 2(e)].

Next, we focus on the p-n junction in which the double negative refraction occurs, as illustrated in Fig. 4. The main features of the transmission coefficients are basically the same as those in positive refraction, except the status of T_1 and T_2 are exchanged. In this case, T_2 dominates the scattering process [see Figs. 4(a) and 4(b)], but T_1 is not very small and it has the same order of T_2. As for the refractive indexes shown in Figs. 4(c) and 4(d), n_1 and n_2 become negative and almost have a mirror symmetry with the positive refractive indexes in Figs. 3(c) and 3(d) about the axis $n = 0$. Contrary to the n-n junction case, two real focal spots are formed at the opposite side of the electron source and the focusing performance of the incident electrons is pretty good [see Fig. 2(f)].

The spin-down electrons show similar refractive behaviors at the two valleys. The double refraction is positive for a n-n junction and negative for a p-n junction, and the absolute value of the refractive index $|n| > 1$ at one valley and $|n| < 1$ at the other. Because of the time reversal invariance of our Hamiltonian, the scattering matrix of the spin-up and spin-down electrons satisfies the relation $\mathbf{s}_\uparrow^T = \mathbf{s}_\downarrow$, which indicates that $T_{1\uparrow} + T_{2\uparrow} = T_{1\downarrow} + T_{2\downarrow}$.

The double negative refraction and double focusing effects can be well demonstrated by plotting the distribution of the local conductance [55,56], as shown in Fig. 5. Let us consider a normal-hexagonal nanoribbon with the interface being located at $x = 0$. Two electrodes (or STMs) respectively couple to the normal and hexagonal regions as the source and detecting electrodes. We assume that the source electrode and the nanoribbon are in contact with four lattices [see the blue area in Fig. 1(a)]. The response signal can be extracted by coupling a detecting electrode locally in the n region, and the detecting electrode is assumed to contact six lattices [see the red area in Fig. 1(a)]. The source electrode in the p region is added a small bias V. The biases of the left terminal (normal conductor), right terminal (hexagonal semiconductor), and detecting electrode are set to zero. Electron flow is injected into the normal conductor from the source electrode located

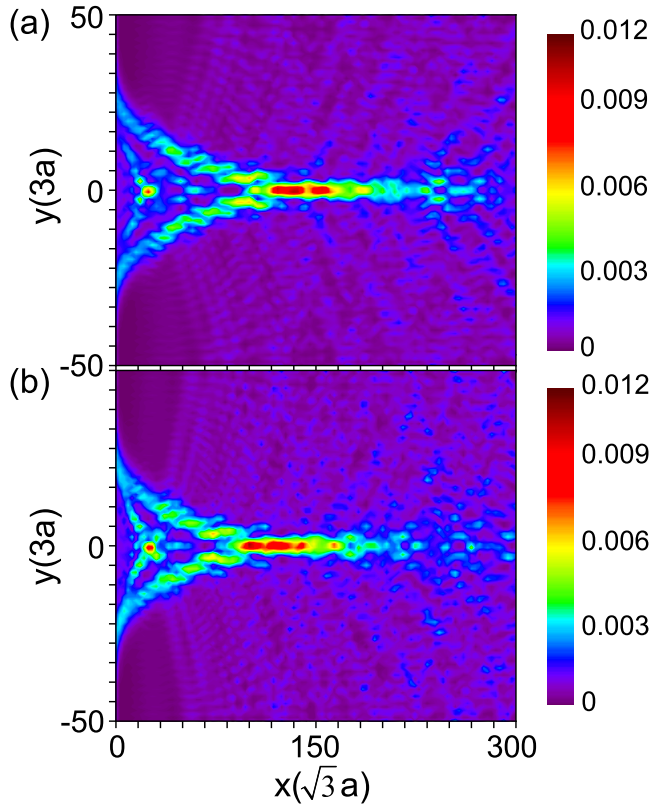

FIG. 5. Distribution of the local conductance in the n region with the p-n interface being located at $x = 0$. The source flow is injected from the square unit cell at $(-150a,0)$. (a) Spin-up electrons undergo double negative refraction when propagating across the junction and are focused in different locations at the n side. Panel (b) is for incident spin-down electrons. The ribbon width is $W = 100 \times 3a$ and the Fermi energy $E = 0$. Other parameters are the same as those in Fig. 4.

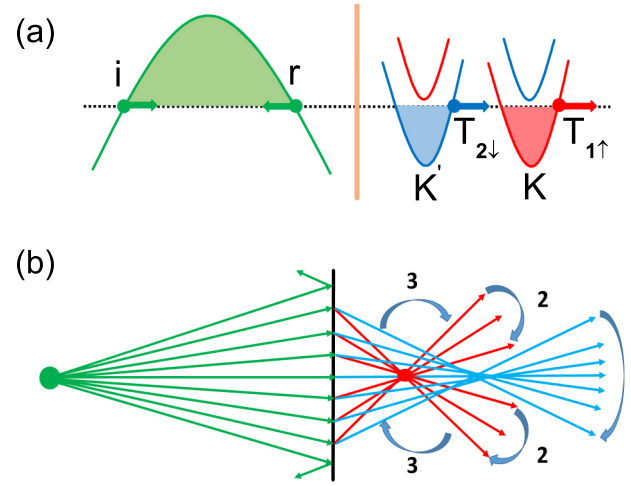

FIG. 6. Spin splitter based on the normal-hexagonal p-n junction. Panel (a) is the band diagrams of the spin splitter. Here the Fermi energy E is located between the energy bands of the spin-up and spin-down species in the n region. Panel (b) is the schematic diagram of the electrons' trajectories in the spin splitter. Electrons with different spin are separated in real space and are focused in different regions.

at $(-150a,0)$ in the p region. The injected electrons spread in all directions and the left-going electrons finally escape because of the open boundary condition. The right-going electrons undergo double refraction and are focused in different locations when propagating across the p-n junction. Below, we study the local conductance flowing from the source electrode to the detecting electrode. The calculation details are presented in Appendix E. As shown in Fig. 5(a), the incident spin-up electrons undergo double negative refraction when propagating across the p-n junction and are focused in different locations at the n side. For the transmission mode 1, the electrons are focused around the spot located at $(25\sqrt{3}a,0)$ and the focusing performance is pretty good, while for the transmission mode 2, the electrons are focused around the area located at $(130\sqrt{3}a,0)$. The refractive index of each mode can be estimated as $n_1 \approx -25\sqrt{3}a/150a = -0.29$ and $n_2 \approx -130\sqrt{3}a/150a = -1.50$, which are consistent with the above theoretical results [see Figs. 4(c) and 4(d)]. The conductance strength of mode 2 is well above that of mode 1, in line with theoretical expectation [see Figs. 4(a) and 4(b)]. For incident spin-down electrons in Fig. 5(b), the local conductance pattern shows similar behaviors. The double negative refraction also occurs and the refractive index $|n| < 1$ at one focal spot and $|n| > 1$ at the other. Note that, besides the focal spots (red regions), there is also an interference pattern (blue wave pattern) shown in Fig. 5. This interference pattern is due to the interference between the two outgoing modes. In a word, the local conductance patterns clearly confirm the double refraction and double focusing effects and all the results are consistent with the theoretical results. In addition, in Appendixes A and B, we also show that the double refraction and double focusing effects are very robust and they are not affected by the coupling Hamiltonian and the parameters of the normal conductor.

IV. SPIN SPLITTER AND DETECTIVE DEVICE

Spin-orbit coupling modifies the electronic band structures at the two valleys and the double refraction becomes spin dependent as mentioned above. Thus, for spin nonpolarized incident electrons from the left side, the outgoing electrons on the right side will be spin polarized, i.e., the normal-conductor/hexagonal-semiconductor junction can be used as a spin splitter. Below, as an example, we consider the p-n junction system and the energy bands are shown in Fig. 6(a). Here the red lines denote the energy bands of spin-up electrons in the n region, while the blue lines denote spin-down ones, and the green lines are the bands in the p region where the spin-up and spin-down electrons are degenerate. In order to clearly illustrate the physical picture of the spin splitter, the Fermi energy E is located between the red line and blue line [see Fig. 6(a)]. In this case, the incident spin-up electrons can only get through the junction via valley K at the state $T_{1\uparrow}$, while the spin-down electrons via valley K' at the state $T_{2\downarrow}$. Notice the states $T_{1\uparrow}$ and $T_{2\downarrow}$ are not mutually the time-reversal states and the dispersion relations at the two valleys $\epsilon_{K\uparrow}(\mathbf{k}-\mathbf{K}) \neq \epsilon_{K'\downarrow}(\mathbf{k}-\mathbf{K}')$, although the system possesses the time-reversal symmetry with the dispersion relations $\epsilon_{K\uparrow}(\mathbf{k}-\mathbf{K}) = \epsilon_{K'\downarrow}(-\mathbf{k}-\mathbf{K}')$. So the refractive indexes of the two valleys are different, leading to the fact that

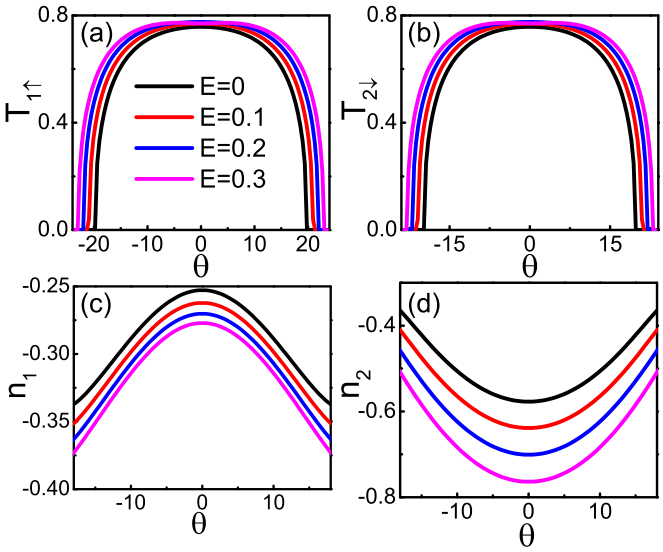

FIG. 7. Transmission coefficients and refractive indexes of the spin splitter. Panels (a) and (b) are the transmission coefficients $T_{1\uparrow}$ and $T_{2\downarrow}$ for spin-up and spin-down electrons, respectively. Panels (c) and (d) are the corresponding refractive indexes. The parameters are $\epsilon_R = -4.2$, $t_R = 8$, $\beta = 4$, $\beta_s = -0.1$, $\epsilon_L = -7$, and $t_L = 8$.

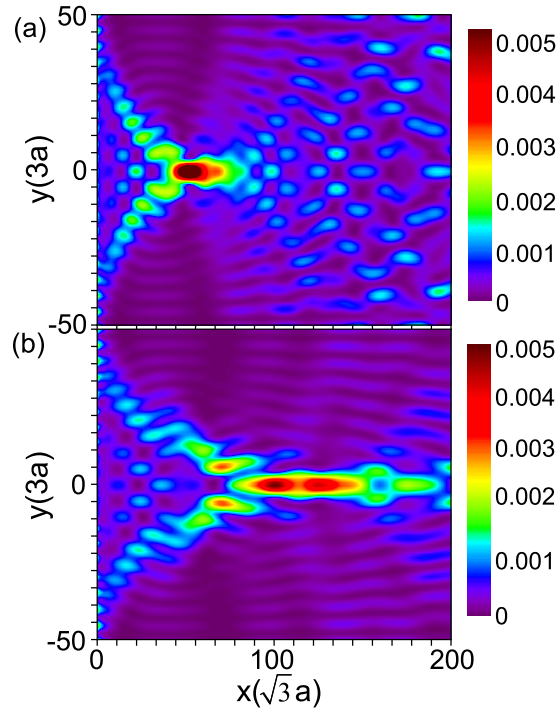

FIG. 8. Distribution of the local conductance in the n region with the p-n interface being located at $x = 0$. The source flow is injected from the square unit cell at $(-300a,0)$. (a) Spin-up electrons are focused around the spot located at $(53\sqrt{3}a,0)$. (b) Spin-down electrons are focused in a relatively large area near $(100\sqrt{3}a,0)$. The ribbon width is $W = 100 \times 3a$ and the Fermi energy $E = 0$. Other parameters are the same as those in Fig. 7.

the electrons with different spin are separated in real space and are focused in different regions. By detailed calculation of the incident and refraction angles, we plot the schematic diagram of the electrons' trajectories in Fig. 6(b). Spin-up electrons are focused around a small spot, while spin-down electrons are focused in a relatively large area. The electron's outgoing area can be divided into three regions. In region 1, both spin-up and spin-down electrons can be observed, but spin-down electrons are in the majority. In region 2, only spin-up outgoing electrons could be observed. In region 3, we can hardly detect any outgoing electron. In particular, at two focal spots the density of the spin-up and spin-down outgoing electrons is very high, which can be detected by using ferromagnetic STM. Note that here the spin-up and spin-down electrons are at the valleys K and K', respectively. So the spin splitter also serves as a valley splitter.

Let us study the transmission coefficients and refractive indexes of the spin splitter. Figures 7(a) and 7(b) are the transmission coefficients $T_{1\uparrow}$ and $T_{2\downarrow}$ of the two transport channels. The two transmission coefficients are in fact identical for various incident energy. This is because for each spin there is only one transmission mode and the general relation $T_{1\uparrow} + T_{2\uparrow} = T_{1\downarrow} + T_{2\downarrow}$ reduces to $T_{1\uparrow} = T_{2\downarrow}$ in the present case. $T_{1\uparrow}$ and $T_{2\downarrow}$ are the maximum when the incident angle $\theta = 0$. With the increase of θ, they decrease. At large θ, $T_{1\uparrow}$ and $T_{2\downarrow}$ rapidly drop to zero. However, due to the band structures at the two valleys being not completely the same, the refractive indexes present different behavior, as illustrated in Figs. 7(c) and 7(d). With larger incident angle, the refractive index n_1 decreases, while n_2 shows opposite behavior. The refractive index n_1 approximately follows the asymptotic behavior of perfect lens and the spin-up electrons are focused around a small spot. However, n_2 obviously do not follow the law and the spin-down electrons are focused in a relatively large area. Note that by changing the spin-orbit coupling constant β_s, different types of focusing patterns can be realized.

To confirm the effectiveness of the spin splitter device, we also present the distribution of the local conductance in the n region, as shown in Fig. 8. Nonpolarized electrons are injected from an electron source located at $(-300a,0)$ at the normal-conductor side, and they are focused in different locations for different spin orientations. In Fig. 8(a), the spin-up electrons are focused around the spot located at $(53\sqrt{3}a,0)$. The corresponding refractive index n_1 can be estimated as $n_1 \approx -53\sqrt{3}a/300a = -0.30$, which is in accord with the-oretical results [see Fig. 7(c)]. However, in Fig. 8(b), the spin-down electrons are focused in a relatively large area near $(100\sqrt{3}a,0)$. The corresponding refractive index n_2 is approximately $n_2 \approx -100\sqrt{3}a/300a = -0.58$, in line with expectations [see Fig. 7(d)]. Therefore, the local conductance patterns are excellently coincident with the schematic diagram discussed in Fig. 6, which strengthens our conclusions of the spin splitter device. Note that in the previous works of spin lens devices, electrons with a certain spin direction are focused, while electrons with other spin directions diverge [14,15]. Here, due to the novel spin-valley locking band structures of the hexagonal lattice, the spin splitter can focus both spin-up and spin-down electrons in different locations in real space. We also notice that, in a recent work [57], the authors proposed the birefringent electron optics in circular doping-controlled graphene in the presence of Rashba spin-orbit interaction.

However, their device cannot be used as a spin splitter because of the possible spin-flip process.

V. SUMMARY

In conclusion, we have proposed a model to realize double refraction and double focusing of electric current using a normal-conductor/hexagonal-semiconductor junction. By breaking the A-B sublattice symmetry and introducing the spin-orbit interaction, a large energy gap is formed and spin-up and spin-down electrons experience opposite effective magnetic field at the two valleys. Incident electrons transmit to the two valleys and result in the double refraction at the hexagonal lattice side. The double refraction can be either positive or negative, depending on the junction being n-n type or p-n type. The two valleys reveal different types of refractive behaviors. The absolute value of the refractive index $|n| > 1$ at one valley and $|n| < 1$ at the other. Additionally, the p-n junction can be used as a spin splitter (valley splitter), which could be verified by the ferromagnetic STM. We also present the local conductance patterns to strengthen the above conclusions. Our results may be useful for the engineering of double lenses in electronic systems and have underlying applications in spintronics.

ACKNOWLEDGMENTS

This work was financially supported by National Key R and D Program of China (No. 2017YFA0303301), NBRP of China (No. 2015CB921102), NSF-China under Grants No. 11574007 and No. 11274364, and the Key Research Program of the Chinese Academy of Sciences (Grant No. XDPB08-4).

APPENDIX A: EFFECT OF THE SQUARE LATTICE AND COUPLING HAMILTONIAN ON THE DOUBLE REFRACTION AND DOUBLE FOCUSING EFFECTS

In this Appendix, we show that the double refraction and double focusing effects do not rely on the detailed forms of the square lattice Hamiltonian H_L and the coupling Hamiltonian H_T. In the main text, the nearest-neighbor distance of the square lattice is $3a/2$ and all the atoms of the outermost layer of the square lattice have a hopping term connecting with the armchair edge of the hexagonal lattice [see Fig. 1(a)]. Here we consider the other two lattice diagrams in Figs. 9(a) and 9(b), where the nearest-neighbor distance of the square lattice is a. The corresponding local conductance patterns for the incident spin-up electrons are shown in Figs. 9(c) and 9(d). Detailed formalism for calculating the local conductance is in Appendix E. The main features of the local conductance patterns are the same as those in Fig. 5 in the main text. Two focal spots obviously emerge. One spot is close to the interface $x = 0$ with the refractive index $|n_1| < 1$ and the focusing performance is pretty good. The other spot is located around $(100\sqrt{3}a,0)$ with the refractive index $n_2 \approx -1$. Here the refractive indexes and the specific interference patterns are slightly different from those in the main text, because of the lattice constant of the square lattice being changed.

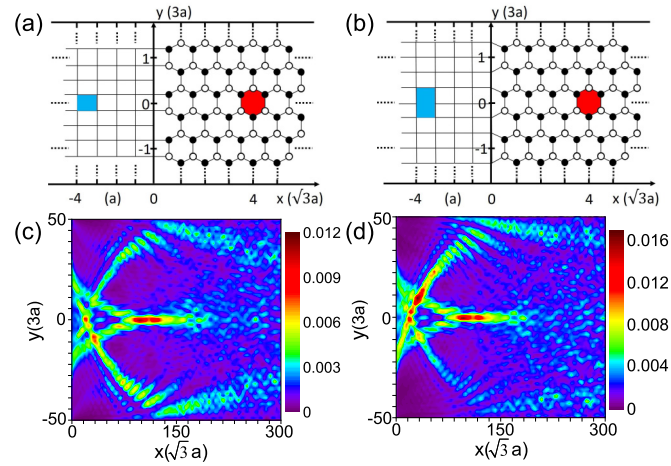

FIG. 9. Panels (a) and (b) are the schematic diagrams of two other types of square-hexagonal-semiconductor junctions. The p-n interface is located at $x = 0$. In (a) the source electrode is in contact with four lattices in the normal conductor, but in contact with six lattices in (b). (c),(d) Distribution of local conductance calculated from the lattice diagram in (a) and (b), respectively. The source flow is injected from the square unit cell at $(-175a,0)$. The ribbon width is $W = 100 \times 3a$, the coupling strength $t_c = t_L = 8$, and the Fermi energy $E = 0$. Other parameters are the same as those in Fig. 5.

However, the double refraction and double focusing effects can always occur. In addition, the local conductance patterns and the focal spots can always be observed as the coupling strength t_c changes (no shown here). In short, the double refraction and double focusing effects can well persist and they do not rely on the detailed forms of H_L and H_T.

APPENDIX B: EFFECT OF t_L AND ϵ_L OF THE NORMAL CONDUCTOR ON THE DOUBLE REFRACTION AND DOUBLE FOCUSING EFFECTS

In this Appendix, we also show that the double refraction and double focusing effects do not rely on the detailed values of t_L and ϵ_L of the normal conductor. In the calculation of the local conductance patterns in Fig. 5 in the main text, the parameters of the normal conductor are set as $t_L = t_c = 8$ and $\epsilon_L = -7$. Here, we keep the coupling strength $t_c = 8$ and study the dependence of local conductance patterns on other values of t_L and ϵ_L. The results are shown in Fig. 10, and (a)–(d) correspond to (t_L, ϵ_L) being $(4, -7)$, $(16, -7)$, $(8, -3.5)$, and $(8, -14)$, respectively. As t_L or ϵ_L changes, the energy dispersion relation of the normal conductor changes accordingly, which leads to different focal positions at the hexagonal lattice side [see Figs. 10(a)–10(d)]. However, the local conductance strength changes little, and the double refraction and double focusing effects can always be observed. Note that the hexagonal lattice have the same band structure with the TMDs [see Fig. 1(d)] and this band structure is totally different from that in graphene. Thus the insulating behavior in normal-conductor/graphene/normal-conductor junctions will not present in our system [50].

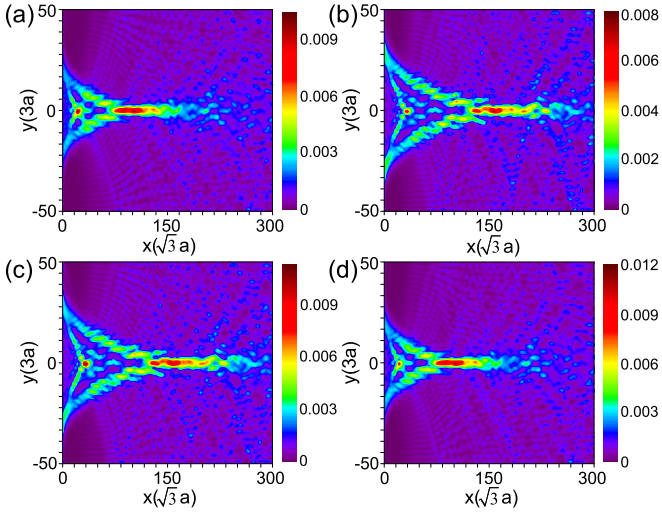

FIG. 10. Effects of t_L and ϵ_L are present. In the calculation of the local conductance patterns in Fig. 5 in the main text, the parameters of the normal conductor are set as $t_L = t_c = 8$ and $\epsilon_L = -7$. Here, we keep $t_c = 8$ and display a local conductance pattern of spin-up electrons for other values of t_L and ϵ_L, with (t_L, ϵ_L) being (4, −7), (16, −7), (8, −3.5), and (8, −14) in (a)–(d), respectively. Other parameters are the same as those in Fig. 5.

APPENDIX C: INCIDENT AND REFRACTION ANGLE

In this Appendix, we will elaborate the definition of the incident and refraction angles in detail. By applying the Bloch theorem to the tight binding Hamiltonian in Eq. (2), the energy band of the normal conductor can be readily derived as

$$\epsilon(k_x,k_y) = \epsilon_L + 2t_L \cos\tfrac{3}{2}k_x a + 2t_L \cos\tfrac{3}{2}k_y a, \tag{C1}$$

where $3a/2$ is the nearest-neighbor distance of the square lattice [see Fig. 1(a)]. The group velocity can be obtained from the band structure as

$$v_x = \frac{1}{\hbar}\left[\frac{\partial\epsilon}{\partial k_x}\right]_{k_y} = -\frac{3at_L}{\hbar}\sin\frac{3}{2}k_x a, \tag{C2}$$

$$v_y = \frac{1}{\hbar}\left[\frac{\partial\epsilon}{\partial k_y}\right]_{k_x} = -\frac{3at_L}{\hbar}\sin\frac{3}{2}k_y a. \tag{C3}$$

Consider a spin-up electron incident from the normal conductor with energy E and transverse wave vector $k_y^{\rm in}$; the wave vector $k_x^{\rm in}$ can be uniquely determined by the condition $v_x > 0$ and Eq. (C1) as

$$k_x^{\rm in}\left(k_y^{\rm in}\right) = \frac{2}{3a}\arccos\frac{E - \epsilon_L - 2t_L\cos\frac{3}{2}k_y^{\rm in}a}{2t_L}. \tag{C4}$$

Because the incident energy $E = 0$ is given, $k_x^{\rm in}$ is only dependent on the transverse wave vector $k_y^{\rm in}$. The incident angle θ of the spin-up electron can be defined as

$$\theta\left(k_y^{\rm in}\right) = \arctan\frac{v_y^{\rm in}}{v_x^{\rm in}} = \arctan\frac{\sin\frac{3}{2}k_y^{\rm in}a}{\sin\frac{3}{2}k_x^{\rm in}a}. \tag{C5}$$

Note that θ is also only dependent on $k_y^{\rm in}$. By sweeping $k_y^{\rm in}$ from $-2\pi/3a$ to $+2\pi/3a$, we obtain different incident angles of incident electrons.

For the hexagonal-lattice material, the energy bands near the K (K') valley can be solved numerically as $\epsilon_{K(K')\sigma}(k_x,k_y)$, where $\sigma = \uparrow, \downarrow$ denotes the electron's spin. Note that there are three conservation laws in the present 2D scattering system. First, there exists the conservation of energy because the Hamiltonian in Eq. (1) is independent of the time. Then, the transverse momentum k_y is conserved as a result of the translational invariance along the y direction. Finally, the spin in the z direction is conserved due to the Pauli matrix σ_z commuting with the Hamiltonian. By combining these conservation laws with the condition $v_{x,K(K')}^{out} = \frac{1}{\hbar}\frac{\partial\epsilon_{K(K')\sigma}}{\partial k_x} > 0$, the wave vector $k_{x,K(K')}^{out}$ at K (K') valley can be uniquely determined from the equation $\epsilon_{K(K')\uparrow}(k_x,k_y^{\rm in}) = E$ ($k_{x,K(K')}^{out}$ is also only dependent on $k_y^{\rm in}$). Then, the refraction angle at K (K') valley is given by

$$\theta_{K(K')}\left(k_y^{\rm in}\right) = \arctan\frac{v_{y,K(K')}^{out}}{v_{x,K(K')}^{out}} = \arctan\left[\frac{\partial\epsilon_{K(K')\uparrow}/\partial k_y}{\partial\epsilon_{K(K')\uparrow}/\partial k_x}\right]_{(k_x,k_y)=(k_{x,K(K')}^{out},k_y^{\rm in})}. \tag{C6}$$

Therefore, corresponding to every incident electron with definite transverse wave vector $k_y^{\rm in}$, we can define the incident angle $\theta(k_y^{\rm in})$ and refraction angle $\theta_{K(K')}(k_y^{\rm in})$.

APPENDIX D: CONDITION FOR PERFECT FOCUS

Consider an electron source located at $(-L,0)$ in the p region. Electrons emitted from the electron source undergo negative refraction at the p-n junction interface, and two real focal spots are formed at $(L_i,0)$ $(i = 1,2)$ in the n region. The geometrical relationship gives

$$\frac{\tan\theta}{\tan\theta_i} = -\frac{L_i}{L}, \tag{D1}$$

where θ is the incident angle and θ_i is the refraction angle of mode i. By using the definition of the refractive index $n_i = \sin\theta/\sin\theta_i$, the above equation can be simplified to

$$n_i^2 = \frac{L_i^2}{L^2} + \left(1 - \frac{L_i^2}{L^2}\right)\sin^2\theta. \tag{D2}$$

By defining $c \equiv L_i^2/L^2$, Eq. (D2) finally reduces to the condition for perfect focus in the main text.

APPENDIX E: LOCAL CONDUCTANCE

In this Appendix, we present the formalism for calculating the local conductance. We consider a normal-hexagonal nanoribbon with a source electrode coupled to the normal-conductor side and a detecting electrode coupled to the right hexagonal region [see Fig. 1(a)]. The source electrode is added a small bias V. The biases of the normal conductor, hexagonal semiconductor, and detecting electrode are set to zero. By using the nonequilibrium Green's function method, the current flowing from the source electrode s to the detecting electrode d can be expressed as

$$I_d = \frac{e}{\hbar}\int\frac{dE}{2\pi}T_{d,s}(E)[f_d(E) - f_s(E)], \tag{E1}$$

where $T_{d,s}(E) = \mathrm{Tr}[\mathbf{\Gamma}_d \boldsymbol{G}^r(E)\mathbf{\Gamma}_s \boldsymbol{G}^a(E)]$ is the transmission coefficient from the source electrode to the detecting electrode. Here, $\boldsymbol{G}^r = \boldsymbol{G}^{a\dagger}$ is the retarded Green's function in the scattering region and $\mathbf{\Gamma}_{s/d} = i(\Sigma^r_{s/d} - \Sigma^{r\dagger}_{s/d})$ is the linewidth function. $f_{s/d}(E)$ in Eq. (E1) is the Fermi distribution function of the source and detecting electrodes, with $f_s(E) = f_0(E - eV)$, $f_d = f_0(E)$, and $f_0(E) = 1/\{\exp(E/k_B\mathcal{T}) + 1\}$. In the low temperature $\mathcal{T}$ and small bias V limits, the local conductance contributed by the source electrode can be written as

$$G = \frac{I_d}{V} = \frac{e^2}{h} T_{d,s}(E_F). \tag{E2}$$

By sweeping the detecting probe in the n region, the distribution of the local conductance can be obtained, as shown in Figs. 5, and 8–10.

[1] S. Datta, *Electronic Transport in Mesoscopic Systems* (Cambridge University Press, Cambridge, England, 1995).
[2] W. van Haeringen and D. Lenstra, *Analogies in Optics and Microelectronics* (Kluwer Academic Punlishers, Netherlands, 1990).
[3] U. Sivan, M. Heiblum, C. P. Umbach, and H. Shtrikman, Phys. Rev. B **41**, 7937 (1990).
[4] J. Spector, H. L. Stormer, K. W. Baldwin, L. N. Pfeiffer, and K. W. West, Appl. Phys. Lett. **56**, 1290 (1990).
[5] C. W. J. Beenakker and H. van Houten, Solid State Phys. **44**, 1 (1991).
[6] P. Lv, A. M. Guo, H. Y. Li, C. X. Liu, X. C. Xie, and Q.-F. Sun, Phys. Rev. B **95**, 104516 (2017).
[7] H. van Houten, C. W. J. Beenakker, J. G. Williamson, M. E. I. Broekaart, P. H. M. van Loosdrecht, B. J. van Wees, J. E. Mooij, C. T. Foxon, and J. J. Harris, Phys. Rev. B **39**, 8556 (1989).
[8] A. Yacoby, U. Sivan, C. P. Umbach, and J. M. Hong, Phys. Rev. Lett. **66**, 1938 (1991).
[9] V. V. Cheianov, V. Fal'ko, and B. L. Altshuler, Science **315**, 1252 (2007).
[10] C.-H. Park, Y.-W. Son, L. Yang, M. L. Cohen, and S. G. Louie, Nano Lett. **8**, 2920 (2008).
[11] M. S. Jang, H. Kim, Y.-W. Son, H. A. Atwater, and W. A. Goddard, Proc. Natl. Acad. Sci. U.S.A. **110**, 8786 (2013).
[12] P. Rickhaus, P. Makk, M.-H. Liu, K. Richter, and C. Schönenberger, Appl. Phys. Lett. **107**, 251901 (2015).
[13] R. D. Y. Hills, A. Kusmartseva, and F. V. Kusmartsev, Phys. Rev. B **95**, 214103 (2017).
[14] A. G. Moghaddam and M. Zareyan, Phys. Rev. Lett. **105**, 146803 (2010).
[15] M. Yang, Y.-K. Bai, W.-L. Zhang, and R.-Q. Wang, Phys. Rev. B **94**, 075433 (2016).
[16] P. E. Allain and J. N. Fuchs, Eur. Phys. J. B **83**, 301 (2011).
[17] V. H. Nguyen, S. Dechamps, P. Dollfus, and J.-C. Charlier, Phys. Rev. Lett. **117**, 247702 (2016).
[18] M. Farokhnezhad, M. Esmaeilzadeh, and Kh. Shakouri, Phys. Rev. B **96**, 205416 (2017).
[19] S.-G. Cheng, Y. Xing, J. Wang, and Q.-F. Sun, Phys. Rev. Lett. **103**, 167003 (2009).
[20] Y. Xing, J. Wang, and Q.-F. Sun, Phys. Rev. B **83**, 205418 (2011).
[21] V. G. Veselago, Sov. Phys. Usp. **10**, 509 (1968).
[22] J. B. Pendry, Phys. Rev. Lett. **85**, 3966 (2000).
[23] S. Guan, S. Y. Huang, Y. Yao, and S. A. Yang, Phys. Rev. B **95**, 165436 (2017).
[24] V. M. Shalaev, Nat. Photon. **1**, 41 (2007).
[25] R. A. Shelby, D. R. Smith, and S. Schultz, Science **292**, 77 (2001).
[26] S. Chen, Z. Han, M. M. Elahi, K. M. M. Habib, L. Wang, B. Wen, Y. Gao, T. Taniguchi, K. Watanabe, J. Hone, A. W. Ghosh, and C. R. Dean, Science **353**, 1522 (2016).
[27] A. H. Castro Neto, F. Guinea, N. M. R. Peres, and K. S. Novoselov, Rev. Mod. Phys. **81**, 109 (2009).
[28] L.-J. Yin, K.-K. Bai, W.-X. Wang, S.-Y. Li, Y. Zhang, and L. He, Front. Phys. **12**, 127208 (2017).
[29] P. Rickhaus, R. Maurand, M. H. Liu, M. Weiss, K. Richter, and C. Schönenberger, Nat. Commun. **4**, 2342 (2013).
[30] A. F. Young and P. Kim, Nat. Phys. **5**, 222 (2009).
[31] G.-H. Lee, G.-H. Park, and H.-J. Lee, Nat. Phys. **11**, 925 (2015).
[32] J.-C. Chen, X. C. Xie, and Q.-F. Sun, Phys. Rev. B **86**, 035429 (2012).
[33] X. X. Xi, Z. F. Wang, W. W. Zhao, J.-H. Park, K. T. Law, H. Berger, L. Forró, J. Shan, and K. F. Mak, Nat. Phys. **12**, 139 (2016).
[34] Y. Saito, Y. Nakamura, M. S. Bahramy, Y. Kohama, J. Ye, Y. Kasahara, Y. Nakagawa, M. Onga, M. Tokunaga, T. Nojima, Y. Yanase, and Y. Iwasa, Nat. Phys. **12**, 144 (2016).
[35] J. M. Lu, O. Zheliuk, I. Leermakers, N. F. Q. Yuan, U. Zeitler, K. T. Law, and J. T. Ye, Science **350**, 1353 (2015).
[36] L. Bawden, S. P. Cooil, F. Mazzola, J. M. Riley, L. J. Collins-McIntyre, V. Sunko, K. W. B. Hunvik, M. Leandersson, C. M. Polley, T. Balasubramanian, T. K. Kim, M. Hoesch, J. W. Wells, G. Balakrishnan, M. S. Bahramy, and P. D. C. King, Nat. Commun. **7**, 11711 (2016).
[37] B. T. Zhou, N. F. Q. Yuan, H.-L. Jiang, and K. T. Law, Phys. Rev. B **93**, 180501(R) (2016).
[38] S.-G. Cheng, Y. X. Xing, Q.-F. Sun, and X. C. Xie, Phys. Rev. B **78**, 045302 (2008).
[39] Q.-F. Sun and X. C. Xie, J. Phys.: Condens. Matter **21**, 344204 (2009).
[40] G. Giovannetti, P. A. Khomyakov, G. Brocks, P. J. Kelly, and J. van den Brink, Phys. Rev. B **76**, 073103 (2007).
[41] L. Kong, C. Bjelkevig, S. Gaddam, M. Zhou, Y. H. Lee, G. H. Han, H. K. Jeong, N. Wu, Z. Zhang, J. Xiao, P. A. Dowben, and J. A. Kelber, J. Phys. Chem. C **114**, 21618 (2010).
[42] S. Gaddam, C. Bjelkevig, S. Ge, K. Fukutani, P. A. Dowben, and J. A. Kelber, J. Phys.: Condens. Matter **23**, 072204 (2011).
[43] R. Skomski, P. A. Dowben, M. S. Driver, and J. A. Kelber, Mater. Horiz. **1**, 563 (2014).
[44] C. L. Kane and E. J. Mele, Phys. Rev. Lett. **95**, 226801 (2005).
[45] Q.-F. Sun and X. C. Xie, Phys. Rev. Lett. **104**, 066805 (2010).
[46] M. Z. Hasan and C. L. Kane, Rev. Mod. Phys. **82**, 3045 (2010).
[47] X.-L. Qi and S.-C. Zhang, Rev. Mod. Phys. **83**, 1057 (2011).
[48] P. Lv, Y.-F. Zhou, N.-X. Yang, and Q.-F. Sun, Phys. Rev. B **97**, 144501 (2018).

[49] J.-L. Ge, T.-R. Wu, M. Gao, Z.-B. Bai, L. Cao, X.-F. Wang, Y.-Y. Qin, and F.-Q. Song, Front. Phys. **12**, 127210 (2017).
[50] J. P. Robinson and H. Schomerus, Phys. Rev. B **76**, 115430 (2007).
[51] Y. M. Blanter and I. Martin, Phys. Rev. B **76**, 155433 (2007).
[52] Y. Mochizuki and H. Yoshioka, J. Phys. Soc. Jpn. **78**, 123701 (2009).
[53] N. Dai and Q.-F. Sun, Phys. Rev. B **95**, 064205 (2017).
[54] S. Sanvito, C. J. Lambert, J. H. Jefferson, and A. M. Bratkovsky, Phys. Rev. B **59**, 11936 (1999).
[55] T. Low, S. Hong, J. Appenzeller, S. Datta, and M. Lundstrom, IEEE Trans. Electron Devices **56**, 1292 (2009).
[56] Y. Xing, J. Wang, and Q.-F. Sun, Phys. Rev. B **81**, 165425 (2010).
[57] M. M. Asmar and S. E. Ulloa, Phys. Rev. B **87**, 075420 (2013).